

Metal telluride-nitride electrocatalysts for sustainably overall seawater electrolysis

Ruopeng Li

Harbin Institute of Technology

Yaqiang Li

Harbin Institute of Technology

Peixia Yang (✉ yangpeixia@hit.edu.cn)

Harbin Institute of Technology

Penghui Ren

Harbin Institute of Technology

Dan Wang

Changzhou University

Xiangyu Lu

Harbin Institute of Technology

Ruoyu Xu

University College London

Yaohua Li

Northwestern University

Junmin Xue

National University of Singapore <https://orcid.org/0000-0003-3349-1873>

Jinqiu Zhang

Harbin Institute of Technology

Maozhong An

Harbin Institute of Technology (HIT)

Jingyuan Ma

Shanghai Advanced Research Institute, Chinese Academy of Sciences

Bo Wang

Harbin Institute of Technology <https://orcid.org/0000-0001-7189-1531>

Hua Liu

University of Wollongong <https://orcid.org/0000-0002-0253-647X>

Shi Xue Dou

University of Wollongong

Keywords: Nanostructured optimization, Heterostructure synergy, Solar and wind-driven, Alkaline seawater electrolysis, Hydrogen evolution

Posted Date: October 29th, 2021

DOI: <https://doi.org/10.21203/rs.3.rs-1007058/v1>

License:  This work is licensed under a Creative Commons Attribution 4.0 International License.

[Read Full License](#)

Abstract

High-efficiency alkaline seawater electrolysis is a promising strategy to promote the sustainability of wide-ranging hydrogen (H_2) production, and the global goal of carbon neutrality. Searching for an ideal candidate with low cost and high electrocatalytic performance for both the hydrogen evolution reaction (HER) and the oxygen evolution reaction (OER) is a major objective. Herein, we report delicate, heterostructured NiTe-NiCoN and NiTe-NiFeN electrocatalysts constructed of nickel cobalt nitride and nickel iron nitride nanosheets uniformly anchored on NiTe nanorod arrays, respectively, which ensure outstanding HER and OER activity along with ultra-long-term stability. Impressively, the NiTe-NiCoN || NiTe-NiFeN couples in alkaline seawater solution delivered 500 mA cm^{-2} at a record low voltage of 1.84 V, and realized an industry-level performance via a solar-powered system and a wind-power system. Further comprehensive analysis has revealed that interface engineering strategy not only ensures that the surficial nitride exposes abundant active sites, but also induces electron modulation that optimizes the binding strength of absorption/desorption for the reaction intermediates to enhanced the the intrinsic activity, as well as facilitate faster electron-mass transfer. Notably, a high electric field intensity generated by the unique nanosheet-nanorod structure induces a local “hydroxide enrichment” environment that effectively promotes the OER kinetics, while inhibits the side effects of chlorine. This work shed lights on these novel heterostructured electrocatalysts with strong synergy, while demonstrating the key role of the unique nanostructures in high-efficiency seawater electrolysis.

Introduction

Hydrogen (H_2) is a promising energy storage medium with the characteristics of ultra-high energy density ($120 \text{ MJ}\cdot\text{kg}^{-1}$) and pro-environment for achieving the goal of carbon neutrality.¹⁻⁵ Compared with traditional steam reforming technology, high-purity H_2 originated from electrical splitting of water, especially, adopting regenerable seawater media (accounting for 96.5% of global water resources), is more sustainable and environmental friendly.⁶⁻¹⁵ Nevertheless, the kinetics limitation due to the sluggish cathodic hydrogen evolution reaction (HER) and the anodic oxygen evolution reaction (OER) results in low electrolysis efficiency, where the competitive alkaline chlorine oxidation reaction (COR, theoretical potential of 1.72 V vs. reversible hydrogen electrode (RHE)) and the chlorine-rich corrosion of the catalyst, are still the main bottlenecks and urgently need to be overcome.¹⁵⁻²⁰

Highly topical research efforts have been committed to exploring efficient non-noble-metal catalysts in the past decade, especially involving 3d-transition metal materials. It is noteworthy that many representative studies have proven that transitional metal nitrides (TMNs) can shrink the d -band of the metal centers, which is positive for the adsorption kinetics of the catalytic intermediate states. Typically, adopting NiCo bimetallic cooperation can accelerate the rate of dissociation/proton active to HER by mobilizing different metal centers, while NiFe can synergistically change the valence state to produce OER promoter of $-OOH$, so as to optimize activity in a targeted manner.^{11,21-29} However, bimetallic nitrides still has a lift space to stimulate catalytic potential, as well as stability. Noting that the interface

engineering of the catalysts could facilitate adaptive synergistic effects to achieve electron modulation that can increase the catalytic performance, it is a feasible strategy to improve the catalytic performance by designing heterogeneous interfaces that are constructed to offer appropriate cooperation with bimetallic nitrides.^{30–34} Among the desired candidates, nickel telluride (NiTe) nanorods array supported on Ni foam (NF) with a higher degree of covalency in the metal-tellurium bond, is significantly different from the strongly polar metal-nitrogen, which will induce the enhanced electronic unsaturation of Ni site at the heterointerface, so as to makes the optimization of the adsorption energy of the reaction intermediates possible and perform as catalytic accelerators. Recently emerging studies of such heterojunctions (NiTe-NiS, NiTe-NiFe(OH)₂, NiTe-RuO₂, NiTe-Ni₂P) have led to a catalytic performance breakthrough, comprehensively proving the beneficial interaction between metallic tellurides and other phases, although studies on the heterojunctions between NiTe and nitrides have not yet been reported.^{35–37}

On the other hand, considering the limitation of anodic reaction rate caused by the slow mass transfer and competitive anion behavior (especially in seawater media), optimizing the catalyst-electrolyte interface properties becomes an effective strategy to improve the catalytic kinetics. Many pioneering studies have found that the direct influence of local electric field changes is directly related to the distribution of interface species and even catalytic performance, especially in self-supported materials.^{38–40} By rationally designing the nanostructures, we expect to build a local ion enrichment mechanism for the electrocatalytic process by changing the electric field conditions, which can increase the hydroxide concentration and suppress the competitive adsorption behavior with chloride ions, thereby addressing the slow OER catalytic kinetics limitation. This may provide novel insights for the design of highly selective seawater electrolysis catalysts, however, systematic studies are still lacking from this perspective.

In this regard, we focus on interface engineering and structural optimization strategies to activate the electrocatalytic performance of nickel-based tellurium and nitrides (Figure 1a, 1b). Based on the activity potential of Ni-Co and Ni-Fe combination, we prepared bimetallic nitride and nickel telluride heterostructured catalysts, NiCoN-NiTe and NiFeN-NiTe with a delicate core-shell nanorod array. Both NiCoN-NiTe and NiFeN-NiTe deliver remarkable HER and OER activity in alkaline solution, respectively. In cooperation, NiTe-NiCoN || NiTe-NiFeN couples, powered by both the solar-electricity and wind-electricity systems, exhibited a record low driving voltage of 1.84 V at the current density of 500 mA·cm⁻² for overall seawater electrolysis, along with operational stability up to 200 h. Further in-depth analysis suggested that the constructed heterojunctions inherited the advantages of NiCo₂N, Ni₃FeN, and NiTe, while the electron modulation regulating optimal adsorption of the reaction intermediates was achieved by interfacial synergy. The NiTe nano-array enabling the active contribution of the bimetallic nitride shell could be abundantly exposed, while ensuring faster electron-mass transportation and rapid gas release, which favors efficient electrocatalysis at high working current density. Significantly, the constructed nanosheet-nanorod nanostructure provides a local “hydroxide enrichment” environment that is caused by strengthening of the local electric field, which strongly promotes OER activity and suppresses the chlorine

side effects in the seawater medium, greatly inspiring the industrial development of hydrogen production by high-performance seawater electrolysis.

Results And Discussion

Synthesis and characteristics of the catalyst materials

A bottom-up route for the synthesis of nickel telluride and metal nitride heterostructures (NiCoN-NiTe and NiFeN-NiTe) is illustrated schematically in **Figure 1c**. Commercial Ni foam serves both as a supporting substrate and metal resource for the NiTe, and the nanorod arrays were uniformly prepared via a hydrothermal method (**Figure 2a**). The following *in-situ* electrochemical deposition process in nickel cobalt or nickel iron nitrate solution realizes the epitaxial growth of NiCo and NiFe hydroxide layers, respectively, with a leaf-like morphology on the NiTe surface. Energy dispersive spectroscopy (EDS) characterization indicated increased distributions of Fe, Co, and O, which proves the element introduction (**Figure S1** in the Supporting Information). Afterwards, the as-prepared NiTe-NiFe(OH)_x and NiTe-NiCo(OH)_x precursors were then heated at 400 °C in an Ar + NH₃ mixed-atmosphere flow to convert them to bimetallic nitrides. The scanning electron microscope (SEM) images and EDS mapping in **Figure 2b, c** and **Figure S2, S3** show that the morphology of the three-dimensional (3D) nanoarray is maintained throughout, and the nitride shells packed with nanosheets are tightly anchored on the NiTe surface with a homogeneous distribution.

Further nanostructured characterization of the as-prepared samples was observed by transmission electron microscopy (TEM). The NiTe crystal plane in **Figure S4** verifies the presence of nickel telluride. Meanwhile, both NiTe-NiCoN and NiTe-NiFeN show similar nanostructures with well-defined heterogeneous interfaces. In the case of the NiTe-NiCoN sample, the NiCo₂N (200) and NiTe (111) facets can be distinctly observed to be in intimate contact (**Figure 2d**) with the lattice spacing of 0.21 nm and 0.31 nm, respectively. The lattice fringes of NiTe-NiFeN in the high-resolution TEM (HRTEM) image of **Figure 2e** exhibit interplanar spacing of 0.31 nm and 0.19 nm, corresponding to NiTe (101) and Ni₃FeN (111) planes, respectively, which is consistent with analysis of the apparent diffraction rings in the selected area electron diffraction (SAED) patterns (**Figure S5**). The corresponding high-angle annular dark field – scanning TEM (HAADF-STEM) elemental mappings and line scan results in **Figure 2f, 2g** directly verify the presence of Ni, Fe, N and Ni, Co, N, as well as the internal enriched distribution of Te. All these characterizations together demonstrate the formation of heterostructured NiTe-NiCoN and NiTe-NiFeN with a delicate 3D core-shell nanostructure.

X-ray diffraction (XRD) was performed to characterize the crystal patterns of all the as-prepared samples. In **Figure 3a**, it is shown that, except for the large diffraction peaks of Ni, the peaks at 31.4°, 43.2°, 46.2°, 56.7°, and 58.6° are completely matched with NiTe (JCPUS 89-2018). After ammoniation, the newly emerged peaks at 41.5°, 48.3°, and 70.6° strongly confirm the final formation of crystalline dual-phase NiFe₃N (JCPUS 50-1434), while the peak at 41.7° of the as-prepared NiCo₂N proves the same evolution. X-ray photoelectron spectroscopy (XPS) was conducted to clarify the surface chemical compositions and

coordinated electronic environment (**Figure 3b-f** and **Figure S6**). All the survey spectra identify the co-existence of Ni and Te, originating from NiTe. Fe, O, and N can be detected on NiTe-NiFeN, and Co, O, and N on NiTe-NiCoN, respectively. The atomic ratio of Ni:Fe:Te:N is $\sim 3:31:20:25:21$, and that of Ni:Co:Te:N is $\sim 3:31:20:25:21$, consistent with the SEM-EDS results but slightly different from the inductively coupled plasma (ICP) results (**Table S1**), which also imply the surficial distribution of N, Co, and Fe. The high-resolution Ni 2p spectra are shown in **Figure 3b**, NiTe exhibits two main peaks for Ni 2p_{3/2} and Ni 2p_{1/2}, which are located at 856.3 and 874.1 eV, and peaks for emerging Ni-N species were identified at 852.4 and 852.3 eV after nitriding.^{21,41} In the Te 3d spectra of **Figure 3c**, two peaks at 572.7 and 582.8 eV correspond to Te²⁻ 3d_{5/2} and Te²⁻ 3d_{3/2}, and a pair of oxidation peaks were also observed, respectively.^{36,42} The Co 2p spectra of NiTe-NiCoN in **Figure 3d** were deconvoluted into Co 2p_{3/2} Co⁰, Co²⁺, and Co³⁺ peaks at 778.6, 780.6, and 786.4 eV, respectively.^{43,44} In the case of NiTe-NiFeN, the Fe 2p_{3/2} and Fe 2p_{1/2} peaks (**Figure 3e**) were located at 711.6 and 724.1 eV.^{11,22} The above results verify the existence of Co and Fe with high valence in nitrides. The N 1s peak (**Figure 3f**) at 398.7 eV is ascribed to the metallic nitrides species, while the peaks at 401.3 eV and 400.6 eV correspond to the N-H bonding.⁴⁵ Significantly, compared with NiTe, a negative binding energy shift of both NiTe-NiCoN and NiTe-NiFeN is shown in the Ni 2p and Te 3d spectra, which appears because the interfacial electron redistribution leads to electron accumulation on the nitrides, generally considered to be beneficial for activating the electrocatalytic properties (details in **Table S2**).^{34,36,46}

X-ray absorption spectroscopy (XAS) was performed to further investigate the electronic structural properties of the heterostructures. In **Figure 3g**, the X-ray absorption near edge spectroscopy (XANES) spectra of the Ni K-edge near-edge structure curves show that the Ni oxidation species coexist in NiTe, NiTe-NiCoN, and NiTe-NiFeN. The NiTe-NiCoN and NiTe-NiFeN exhibit lower energy levels than NiTe, which will cause a low-level shift of the Ni *d*-band center and subsequently reduce the bonding strength of intermediates (H*, *OH, *O, and *OOH) on the catalyst surface, to the benefit of the reaction kinetics.^{36,37} Work-function (WF) tests were carried out by scanning Kelvin probe microscopy (**Figure 3h**). The calculated values of both NiTe-NiFeN (5.11 eV) and NiTe-NiCoN (5.12 eV) are lower than that of NiTe (5.22 eV), suggesting sufficient electron pathways across the heterogeneous interface.⁴⁶ Subsequently, the liquid contact angle and gas evolution angle of different nano-array structures were measured and are compared in **Figure S7**. Evidently, NiTe-NiCoN and NiTe-NiFeN with the array structure have better immersion and gas release behavior, thereby ensuring stable solid-liquid-gas interfaces during the electrocatalytic process. In order to explore the role of the heterogeneous interfaces in depth, we also prepared NiCoN and NiFeN samples without NiTe cores for comparison (labeled as NiCoN-NF and NiFeN-NF, respectively). The SEM images in **Figure S8** show the flat morphology without NiTe support, and the EDS analysis confirms the uniform distribution of metals and nitrogen. The XRD spectra in **Figure S8c** characterize the construction of Ni₃FeN and NiCo₂N with results that are similar to those above. The subsequent electrocatalytic comparisons will visually demonstrate the role of heterogeneous structures.

Electrocatalytic hydrogen and oxygen evolution performance

The advantages of NiTe-NiCoN and NiTe-NiFeN (heterointerface effect, 3D nanostructure, bimetal synergy) offer promising electrocatalysis performance. The alkaline HER activity of NiTe-NiCoN was first evaluated by linear sweep voltammetry measurements (LSV) in a typical three-electrode system, where all the as-prepared samples and a commercial candidate (Pt/C) were also included for comparison. All the curves were corrected by iR compensation (85%). As shown in **Figure 4a**, NiTe-NiCoN exhibits remarkable activity with a small overpotential of 62 and 240 mV to deliver current densities of 10 and 500 mA cm⁻², respectively, which is obviously better than those of NiTe ($\eta_{10} = 274$ mV) and NiCoN-NF ($\eta_{10} = 90$ mV), and comparable to that of Pt/C ($\eta_{10} = 37$ mV). The reaction kinetics of the HER determines the catalytic activity, which can be visualized intuitively through the derived Tafel slope. In **Figure 4b**, the calculated Tafel slope value of NiTe-NiCoN is 48 mV dec⁻¹, which is relatively lower than for NiCoN-NF (95 mV dec⁻¹) and NiTe (198 mV dec⁻¹), indicating that the HER process follows a Volmer–Heyrovsky mechanism with optimized catalytic kinetics. For coupling with NiTe-NiCoN catalyst for efficient overall water electrolysis, we simultaneously examined the OER activity of the as-prepared NiTe-NiFeN and its control group. In **Figure 4d**, NiTe-NiFeN shows exceptional OER activity with a η_{10} of 211 mV and η_{500} of 300 mV, which is much better than for NiFeN-NF ($\eta_{10} = 259$ mV), NiTe ($\eta_{10} = 339$ mV), and IrO₂ ($\eta_{10} = 251$ mV). Meanwhile, the relatively lowest Tafel slope of NiTe-NiFeN (39 mV dec⁻¹) compared with NiFeN-NF (51 mV dec⁻¹) and NiTe (124 mV dec⁻¹) directly verifies the rapid OER kinetics of the heterogeneous interface and bimetal synergy (**Figure 4f**). It is worth mentioning that both NiTe-NiCoN and NiTe-NiFeN are also competitive in recent representative research work (**Table S3**), and further HER performance of NiTe-NiFeN and OER performance of NiTe-NiCoN prove the electrocatalytic pertinence (**Figure S9**).

Further electrochemical analysis were adopted to investigate the properties of all the as-prepared catalysts. The electrochemical surface area (ECSA) calculated from the double-layer capacitance (C_{dl}) was used to evaluate the density of active sites. In **Figure S10**, the derived values of NiTe-NiCoN and NiTe-NiFeN are 38.5 mF cm⁻² and 37.4 mF cm⁻², respectively, which are obviously higher than for NiCoN-NF (19.1 mF cm⁻²), NiFeN (29.3 mF cm⁻²), and NiTe (13.8 mF cm⁻²). The calculated ECSA values intuitively illustrate the enlarged active surface area achieved by the unique core-shell structure. Moreover, the normalized curves also exhibit the best activity of NiTe-NiCoN and NiTe-NiFeN, indicating that factors other than the active surface area are also critical. Assuming that all the loaded metal ions functioned as positive active sites, the turnover frequency (TOF) values were then measured under the HER overpotential of 150 mV. The calculated TOF of NiTe-NiCoN is 0.314 s⁻¹, which is obviously higher than those of NiTe (0.006 s⁻¹), NiCoN (0.132 s⁻¹), and NiTe-Ni₃N (0.065 s⁻¹). Under the overpotential of 300 mV, NiTe-NiFeN exhibits a higher TOF of 0.225 s⁻¹ towards the OER than NiFeN-NF (0.082 s⁻¹) and NiTe (0.005 s⁻¹), suggesting improved intrinsic activity (**Figure S11**). Additionally, electrochemical impedance spectroscopy (EIS) measurements were conducted, and the Nyquist plots are shown in **Figure S12**. The corresponding fitting results in **Table S4** demonstrate that in the HER, NiTe-NiCoN has a lower charge-transfer resistance (R_{ct}) of 3.52 Ω than those of NiCoN-NF (6.47 Ω) and NiTe (53.68 Ω). Similarly, in the OER, NiTe-NiFeN also shows the lowest R_{ct} of 4.64 Ω compared with the other samples (NiFeN-NF: 8.85 Ω , NiTe: 38.4 Ω), as expected, which can be ascribed to the faster electron transport during the HER and OER

processes. Impressively, the integrated radar charts of **Figure 4c** and **4f**, taken together, exhibit the advantages of both NiTe-NiCoN and NiTe-NiFeN, evidently demonstrating the enhanced comprehensive properties that benefit from the rational design of the bimetallic composition as well as the suitable heterostructures.

Moreover, an electrocatalytic operating durability assessment was performed by chronopotentiometric testing under different current densities in 1 M KOH electrolyte. As displayed in **Figure 4g** and **4h**, the best candidates, NiTe-NiCoN and NiTe-NiFeN, exhibited ultra-long stability at 10, 20, 50, 100, and 500 mA cm⁻² without significant attenuation after 60 h of operation. In **Figure S13**, the polarization curves after the stability tests also showed well preserved activity, and the collected SEM images confirmed the good structural stability. Afterwards, the XPS spectra shown in **Figure S14** confirmed the composition integrity. Notably, NiTe-NiCoN and NiTe-NiFeN exhibit obviously decreased surface N and Te distributions, while the emergence of an -OH peak in the O 1s spectrum at 532.1 eV, accompanying by the hydroxide evolution of the nickel-based components, identifies the surface reconstruction evolving the Ni-based species (NiCo-OH and NiFe-OOH).^{47,48} Overall, the above-mentioned analyses prove the successful construction of heterostructured NiTe-NiCoN and NiTe-NiFeN catalyst with promising performance in both the HER and the OER.

Overall seawater electrolysis performance

In order to overcome the constraints of scarce freshwater resources and expand the environmentally-friendly process of water electrolysis, we then investigated the HER and OER performance of our samples in a simulated seawater electrolysis system (1 M KOH + 0.5 M NaCl) and in a real seawater electrolysis system (1 M KOH + natural seawater, only after standing still for 12 h) (**Figure S15**). Under the chloride-rich conditions, the corrosion polarization curves (**Figure S16**) demonstrated that the nitride coating could significantly reduce the corrosion current, which improves the Cl-corrosion resistance to better adapt to the seawater system. LSV measurements were then performed and are shown in **Figure 5a**, where NiTe-NiCoN and NiTe-NiFeN still exhibit HER and OER activity comparable to those pure alkaline solution and have better activity than the other samples (**Figure 5b** and **Figure S17**), and demonstrate excellent catalytic performance when working together. The decline of about 50 mV in the HER and OER in alkaline seawater is due to the hindrance of insoluble impurities (e.g., Ca(OH)₂, Mg(OH)₂) (**Figure S18**).^{8,49} Encouragingly, a non-membraneous two-electrode electrolyzer was built to achieve overall seawater-alkaline electrolysis, which employed the desirable anodic candidates NiTe-NiFeN and NiTe-NiCoN, respectively, to promote the concept of sustainable hydrogen production driven by solar/wind power (**Figure 5c**). In **Figure 5d**, the polarization curves of the NiFeN-NiTe || NiCoN-NiTe couple exhibit the same excellent overall activity in the pure alkaline electrolytes with 1.57 V and 1.75 V required to produce 100 and 500 mA cm⁻², respectively, while it also shows similar performance in alkaline simulated seawater electrolyte. It is noteworthy that this couple required a cell voltage of 1.65 V to deliver 100 mA cm⁻², and 1.84 V at 500 mA cm⁻² in 1 M KOH + seawater electrolyte with IR compensation. Compared with recently reported overall electrolysis performances (**Figure 5d**), the as-constructed couple could be an ideal

candidate for efficient hydrogen production.^{8,13,50-56} The electrocatalytic performance of NiFeN-NiTe || NiCoN-NiTe in further high temperature testing (60°C) shows significantly improved catalytic activity, demonstrating the positive response of reactivity activity to temperature changes, while also suggesting a new direction for heat utilization (**Figure S19**). A self-installed solar-powered system was assembled with an output voltage of 1.9 V (**Figure S20a** and **Video S1**) and actuated by a wind-powered system at about 1.7 V (**Figure S20b** and **Video S2**). All of these systems realized electrolysis of the seawater system, demonstrating that these coupled systems have the potential to utilize renewable energy and provide intermittent storage (solar/wind energy to hydrogen energy).

In **Figure 5e**, the fabricated electrolysis system (with or without the seawater medium) drives 10 mA cm⁻², 100 mA cm⁻², and an industrial current density of 500 mA cm⁻² to investigate the long-term chronopotentiometric response and judge the stability of the catalyst for industrial applications. It can be easily seen that both systems have ultra-long stability of more than 200 h and that the attenuation is within 5%. The calculated Faradaic efficiency (FE) of hydrogen evolution in the simulated seawater full-cell, as measured by both gas chromatography (GC) and drainage gas collection, was approximately 98 % (**Figure 5f**), and the volume ratio of the two-pole product was 2:1 (**Figure S21a**). Subsequently, it was detected by ultraviolet-visible spectroscopy (UV-VIS) that no ClO⁻ was produced after the anode reaction (**Figure S21b**), which confirms the effective inhibition of chlorine oxidation. All these results taken together revealed the excellent energy efficiency and high selectivity in the electrolysis process, confirming the feasibility of the system-integration concept to achieve industrial-scale and environmentally friendly hydrogen production.

Electrocatalytic mechanism analysis

Inspired by this remarkable electrocatalytic performance, density functional theory (DFT) calculations were performed to theoretically reveal the relationship between the synergistic effects of the heterostructure and the intrinsic electrocatalytic activity of both NiTe-NiCoN and NiTe-NiFeN. Generally, the alkaline HER consists of the initial catalyst acting on the H₂O, the intermediate H* adsorption, and the final H₂ desorption. The water oxidation pathway undergoes four coordinated electron transfer steps and generates a series of key oxygenated species (OH*, O*, and OOH*, where the active sites are labeled as *).⁵⁷⁻⁵⁹ Critically, the appropriate atomic sites and interface states determine the reduced thermodynamic barriers. The optimized kinetic models and the adsorbed configurations of the samples to be studied (NiTe, Ni₃FeN, NiTe-NiFeN, NiCo₂N, and NiTe-NiCoN) on the heterojunction surfaces are shown in **Figure S22**. For the calculated H₂O adsorption and the intermediate adsorption energy of H*, NiTe-NiCoN displays a higher $\Delta E_{\text{H}_2\text{O}}$ of -0.61 eV than the NiTe value of -0.11 eV, indicating the strengthened H₂O adsorption for improved water dissociation (**Figure S23**).⁶⁰ In **Figure 6a**, the middle value of the Gibbs free energy, $\Delta G_{\text{H}^*} \approx 0.41$ eV, is better than for NiTe and NiCo₂N, illustrating the favorable H* adsorption kinetics during the HER. In the case of the OER, the Ni site of NiTe undergoes the third electrochemical step (*O → *OOH) with the largest barrier of 2.32 eV, which is the rate-determining step (RDS) that results in slow kinetics. In contrast, the RDS of Ni₃FeN (O* → OOH*) has a barrier of 1.82 eV on the major Ni sites.

In the case of the interfacial NiTe-NiFeN, a significantly lower RDS barrier of 1.71 eV illustrates the optimized OER activity, which is mainly derived from the stronger adsorption of OH* and the favorable stabilization of intermediates (**Figure 6b**). To further explore the laws of adsorption energy change, the density of state (DOS) with the orbitals for different elements was employed for systematic analysis. In **Figure 6c**, the heterojunction *d*-band center is higher than those of NiTe, NiCoN, and NiFeN at the Fermi level, implying that the heterogeneous interface leads to a more rapid electron exchange at the catalyst–intermediate interface, as well as enhanced electron transfer ability, the same as in the impedance analysis. In the simulated electron density distribution (**Figure 6d, 6e**), obvious electron transfers from NiCo₂N to NiTe and from Ni₃FeN to NiTe were examined that were consistent with the above XPS phenomenon, further indicating the enriched electron and hole distributions on metal nitrides. The charge distribution between Ni-N-Co and Ni-N-Fe also show a tendency for electrons to move away from the Ni site and thus gain greater freedom, which favors the optimization of the adsorption energy modulation as well as surface –OOH reconstruction (**Figure S24**).

Previous reports have demonstrated the influence of electric field changes that were guided by nanostructures on the catalytic activity of the cathode (e.g., the CO₂ reduction reaction (CO₂RR) and the HER). As a semi-reaction that limits the efficiency of water electrolysis, the OER performance, structural characteristics, and electric field distribution should be similarly related, and worth systematic exploration. In **Figure S25**, the surface electric field distributions (measured by atomic force microscopy (AFM) and Kelvin probe force microscopy) of the as-prepared NiTe-NiFeN with different calcining temperatures (400 and 475 °C, respectively) together demonstrated that the heterostructured electrocatalyst with uneven surface structure enlarges the charge accumulation. We constructed a simulated electrochemical model of heterostructured nickel telluride and nickel-based nitride based on the TEM and AFM morphology to reveal their influence on anodic catalytic behavior by the finite-element numerical method (details in the Supporting Information). Obviously in **Figure S26a**, the core-shell structure with nanosheet wrapping results in a more uniform and stronger current response than the smooth rod surface, which means that the active site is fully mobilized. The calculated diffusion flux under the two models indicates that the increase in current density promotes the more rapid concentration of hydroxide radicals on the electrode surface (**Figure S26b**). The rich and high-curvature convex structure will generate a local electrostatic field environment, thereby changing the ion migration and distribution states in the electrocatalytic process, which will have a certain impact towards improved OER activity as well as selective anode reactions (OER and CER). Therefore, we comparatively studied the influence of different electric fields on the ion distribution in the Helmholtz layer. It can be seen in **Figure 6f** and **Figure S27** that under the condition of high field strength generated by high curvature, the "hot spot" effect near the electrode area is particularly significant and has more charge accumulation, which results in enhanced local field strength and changes in the anion concentration. Furthermore, the linear relationship between the position of the Helmholtz layer and the electric field intensity, as well as with the ion concentration (**Figure 6g**) directly proves the stronger difference in anion concentration near the electrode surface in the high curvature structure. The OH⁻ concentration is twice as high as that of Cl⁻ (0.2 mol cm⁻³ compared to 0.1 mol cm⁻³ at 0.3 V), but the simulated Helmholtz layer under different potentials

results in the same phenomena for both (**Figure S28**). OH⁻ radicals have a more rapid transfer process, which makes the “hot spot” near the electrode area appear in the hydroxide-rich state and occupy more active sites to ensure rapid oxygen evolution reaction kinetics, as shown in the inset of **Figure 6g**. At the same time, this state can also hinder the adsorption of chloride ions, thereby inhibiting the CER as well as the chlorine corrosion⁶¹. The competition-inhibition effect produced by the nanostructure provides a guarantee of an efficient and stable seawater electrolysis process (**Figure 6h, Figure S29**). To sum up, competitive theoretical simulation analyses demonstrate the synergetic effect of the heterostructure and the nanostructure advantage, which together determine the increased electrocatalytic performance.

Conclusions

In summary, we developed delicate electrocatalysts consisting of NiTe-NiCoN and NiTe-NiFeN via an electrochemical deposition strategy on NiTe nanoarrays to generate precursors and accomplish nitriding under ammonia atmosphere, to serve as active and stable alkaline seawater splitting electrocatalysts. The self-supported catalysts exhibited excellent catalytic performance in both alkaline pure water and natural seawater solutions. The electron modulation, regulating adsorption for the reaction intermediates and optimizing the RDS, was achieved by interfacial synergy between the metal nitride and the nickel telluride. The internally supported NiTe facilitates faster electron-mass transport in the electrodes, an abundant exposed area, and improved wettability as well as rapid gas release pathways. Notably, core-shell structure with the nanorods covered by nanosheets induces the “hot spot” effect that adjusts the electric field state, which results in hydroxide enrichment to promote HER activity and inhibit the CER behavior during seawater oxidation. All these ensure that the HER activity and high selective OER can take place at an industrial operating current density. Inspiringly, NiTe-NiCoN || NiTe-NiFeN couples have exhibited a record low driving voltage, only requiring 1.84 V at the current density of 500 mA cm⁻² for overall seawater electrolysis. Driven by the solar-powered and wind-powered integrated system, the overall electrolysis achieved superior stability and high energy efficiency, paving the way for efficient and environmentally friendly hydrogen production.

Experimental Section

Materials and Chemicals:

Sodium selenite (Na₂TeO₃), hydrazine hydrate (N₂H₄·H₂O, 80%), Ni(NO₃)₂·6H₂O, Fe(NO₃)₃·9H₂O, Co(NO₃)₂·6H₂O, and KOH were purchased from Shanghai Aladdin Biochemical Technology. Pt/C (20 wt%), IrO₂ (99%), and Nafion (5 wt%) were obtained from Johnson Matthey and Dupont, respectively. All chemicals and reagents were used without further purification. Ni foam (thickness: 1.6 mm, porosity: ~95%) was purchased from Kunshan Longsheng. Deionized (DI) water (resistivity: 18.3 MΩ·cm) was used for reaction and pure aqueous solution configuration. The seawater solution used for the tests was collected from Shenzhen Bay, Shenzhen, Guangdong Province, China.

Synthesis of NiTe nanorod array. NiTe was prepared on nickel foam through a typical hydrothermal method 52. A piece of commercial Ni foam ($2 \times 4 \text{ cm}^2$) was cleaned by ultrasonication with acetone and DI water, respectively, then transferred into a Teflon-lined stainless steel autoclave in 20 ml H_2O + 12 ml N_2H_4 , and kept at 180 °C for 24 h. After the reaction, the foam was taken out and washed with deionized water several times, and then dried at 50 °C for 6 h.

Synthesis of NiTe-NiCo(OH)_x, NiTe-NiFe(OH)_x, NiTe-NiCoN, and NiTe-NiFeN nanorod arrays. To prepare NiTe-NiCo(OH)_x and NiTe-NiFe(OH)_x, the NiTe precursor was immersed in 50 ml homogenous aqueous electrolytes containing $\text{Ni}(\text{NO}_3)_2 \cdot 6\text{H}_2\text{O}$ (0.075 M) and $\text{Co}(\text{NO}_3)_2 \cdot 6\text{H}_2\text{O}$ (0.075 M) or $\text{Ni}(\text{NO}_3)_2 \cdot 6\text{H}_2\text{O}$ (0.06 M) and FeSO_4 (0.09 M), respectively. Using a three-electrode system, the electrodeposition potential was -1 V vs. AgCl/Ag, and Pt foil was employed as the counter electrode. After 90 s, the two products were dried under the same conditions as above, and then subjected to a mixed gas nitrating treatment at 400°C for 2 h (120 sccm NH_3 + 30 sccm N_2) with a 5°C/min heating rate, to finally obtain NiTe-NiCoN and NiTe-NiFeN.

Preparation of commercial catalysts on Ni foam. 20 mg of Pt/C and 20 μL of Nafion were dispersed in DI water (230 μL) and isopropanol (250 μL), before being ultrasonicated for 30 min to form a homogeneous catalyst ink. The dispersion was then coated onto an Ni foam substrate, which was dried at room temperature overnight. IrO_2 electrodes were obtained by the same method.

Materials characterization:

The surface morphology, and elemental composition and distribution of the samples were examined by scanning electron microscopy (SEM, ZEISS) and transmission electron microscopy (TEM, FEI Tecnai 30) coupled with energy dispersive X-ray (EDX) spectroscopy. The phase composition of the samples was characterized by X-ray diffraction (Rigaku D/max 2550 VB +18 kW with Cu K α radiation) and X-ray photoelectron spectroscopy (PHI Quantera XPS). X-ray absorption spectra at Ni K-edge was performed on the BL14W1 beam line at the Shanghai Synchrotron Radiation Facility (SSRF), Shanghai Advanced Research Institute, China. Scanning Kelvin probe (SKP) measurements (SKP5050 system, Scotland) were conducted in ambient atmosphere, and gold electrode was used as the reference. The surface potential was detected with an atomic force microscope equipped with Kelvin probe technology (Bruker, Dimension Fastscan03040155).

Electrochemical measurements:

The electrochemical performance was tested on a CHI 660e Electrochemistry Workstation with the standard three-electrode system. The prepared samples were adopted as the working electrode, a graphite rod as the counter electrode, and Hg/HgO electrode as the reference electrode. Different electrolytes (1 M KOH, 1 M KOH + 0.5 M NaCl, 1 M KOH + natural seawater) were adopted with the pH of 13.8. All the linear sweep voltammetry (LSV) polarization curves were acquired at 2 mV s^{-1} with 85% IR compensation. Electrochemical impedance spectroscopy (EIS) measurements were carried out at frequencies ranging

from 10 to 0.001 Hz at -0.1 V (vs. RHE). The double layered capacitances (C_{dl}) of these fabricated electrodes were measured by cyclic voltammetry (CV) curves from -0.1 to 0 V (vs. HgO/Hg) at different scan rates, and the calculated ECSA was estimated from $C_{dl}/0.04$. TOFs calculated by the formula: $TOF = j \times S / (z \times F \times n)$, where j , S , and F correspond to the current density, geometric area, and Faraday's constant (96,485.3 C mol⁻¹) respectively. The z value is 2 and 4 in the HER and the OER, respectively. The n is the molar amount of surficial metals, assuming that every metal atom is involved in the catalysis.

In the overall two-electrode electrolysis, the as-prepared NiTe-NiCoN and NiTe-NiFeN catalysts were used as the anode and cathode, respectively. The polarization curves were measured in different electrolytes at different temperatures (25 and 60 °C), and stability tests were carried out under constant current densities of 10, 100, and 500 mA cm⁻² at room temperature. H₂ Faraday efficiency (FE) is defined from the electrolysis that works at a constant voltage of 2 V (with IR compensation) in a 1 M KOH + 0.5 M NaCl solution, based on the calculated value of the total amount of hydrogen or oxygen and the total reaction charge determined by experiments (including gas chromatography and exhaust gas collection).

Theoretical simulation:

All models were computed based on density-functional theory (DFT), as implemented in the Vienna Ab-initio Simulation package (VASP), and the Perdew-Burke-Ernzerhof (PBE) exchange-correlation functional was applied within the generalized gradient approximation. The reasonable vacuum layers were set around 15 Å in the z-direction to avoid interaction between planes. The cut-off energy and the k-point mesh were 400 eV and 4×4×1, respectively. Geometry optimizations for energy and force were set to 0.02 eV/Å and 10⁻⁵ eV, respectively. The Gibbs free energy provides a sign of spontaneous reaction in the OER. Specifically, the Gibbs free energy can be obtained by adding corrections including entropic (TS) and zero-point energy (ZPE) corrections to calculated DFT energy, so that $\Delta G = \Delta E_{DFT} + \Delta ZPE - T\Delta S - eU$ (5), where the E_{DFT} is the calculated DFT reaction energy, ΔZPE is the change in ZPE calculated from the vibrational frequencies, ΔS is the change in entropy, referring to thermodynamics databases, and U is the Hubbard term.

COMSOL multiphysics simulations:

The simulation was carried out using the COMSOL Multiphysics finite-element-based solver. A single nanowire model with nanosheets randomly distributed on the surface was built up as anode, which represented the electrocatalytic material that we prepared, while a single nanowire model without nanosheets was used as the control sample, as is shown in Figure 6f. Electrostatics and Transport of diluted species modules were coupled together to establish the electrical double layer according to the Gouy-Chapman-Stern model, which consists of a Helmholtz layer and a diffusion layer, in order to obtain the electric field and ion distribution near the electrodes, as well as the free electron density within the electrodes, while the Electrochemical module was used to solve for the reaction current density. Details are shown in the Supporting Information.

References

1. Dawood, F., Anda, M. & Shafiullah, G. M. Hydrogen production for energy: An overview. *Int. J. Hydrog. Energy* **45**, 3847–3869 (2020).
2. Chen, L., Dong, X. L., Wang, Y. G. & Xia, Y. Y. Separating hydrogen and oxygen evolution in alkaline water electrolysis using nickel hydroxide. *Nat. Commun.* **7**, 11741 (2016).
3. Abe, J. O., Popoola, A. P. I., Ajenifuja, E. & Popoola, O. M. Hydrogen energy, economy and storage: Review and recommendation. *Int. J. Hydrog. Energy* **44**, 15072–15086 (2019).
4. Hu, C. G. & Dai, L. M. Multifunctional Carbon-Based Metal-Free Electrocatalysts for Simultaneous Oxygen Reduction, Oxygen Evolution, and Hydrogen Evolution. *Adv. Mater.* **29**, 164902 (2017).
5. Suryanto, B. H. R., Wang, Y., Hocking, R. K., Adamson, W. & Zhao, C. Overall electrochemical splitting of water at the heterogeneous interface of nickel and iron oxide. *Nat. Commun.* **10**, 5599 (2019).
6. Tian, X. Y., Zhao, P. C. & Sheng, W. C. Hydrogen Evolution and Oxidation: Mechanistic Studies and Material Advances. *Adv. Mater.s* **31**, 1808066 (2019).
7. Hu, C. L., Zhang, L. & Gong, J. L. Recent progress made in the mechanism comprehension and design of electrocatalysts for alkaline water splitting. *Energy Environ. Sci.* **12**, 2620–2645 (2019).
8. Kuang, Y. *et al.* Solar-driven, highly sustained splitting of seawater into hydrogen and oxygen fuels. *Proc. NatlAcad. Sci. USA* **116**, 6624-6629 (2019).
9. Dutta, S., Indra, A., Feng, Y., Han, H. & Song, T. Promoting electrocatalytic overall water splitting with nanohybrid of transition metal nitride-oxynitride. *Appl. Catal. B* **241**, 521–527 (2019).
10. Huang, L. L. *et al.* Zirconium-Regulation-Induced Bifunctionality in 3D Cobalt-Iron Oxide Nanosheets for Overall Water Splitting. *Adv. Mater.* **31**, 1901439 (2019).
11. Yu, L. *et al.* Non-noble metal-nitride based electrocatalysts for high-performance alkaline seawater electrolysis. *Nat. Commun.* **10**, 5106 (2019).
12. Huang, Y. C. *et al.* Nitrogen treatment generates tunable nanohybridization of Ni₅P₄ nanosheets with nickel hydr(oxy)oxides for efficient hydrogen production in alkaline, seawater and acidic media. *Appl. Catal. B* **251**, 181–194 (2019).
13. Yu, L. *et al.* Ultrafast room-temperature synthesis of porous S-doped Ni/Fe (oxy)hydroxide electrodes for oxygen evolution catalysis in seawater splitting. *Energy Environ. Sci.* **13**, 3439–3446 (2020).
14. Liu, C. *et al.* A half-wave rectified alternating current electrochemical method for uranium extraction from seawater. *Nat. Energy* **2**, 17007 (2017).
15. Dresp, S., Dionigi, F., Klingenhof, M. & Strasser, P. Direct Electrolytic Splitting of Seawater: Opportunities and Challenges. *Acs Energy Lett.* **4**, 933–942 (2019).
16. Jin, H. Y. *et al.* Stable and Highly Efficient Hydrogen Evolution from Seawater Enabled by an Unsaturated Nickel Surface Nitride. *Adv. Mater.* **33**, 2007508 (2021).
17. Yu, Z. Y. *et al.* Clean and Affordable Hydrogen Fuel from Alkaline Water Splitting: Past, Recent Progress, and Future Prospects. *Adv. Mater.* **33**, 2007110 (2021).

18. Sun, F. *et al.* Energy-saving hydrogen production by chlorine-free hybrid seawater splitting coupling hydrazine degradation. *Nat. Commun.* **12**, 4182 (2021).
19. Tong, W. *et al.* Electrolysis of low-grade and saline surface water. *Nat. Energy* **5**, 367–377 (2020).
20. Li, R. P. *et al.* Electrodeposition: Synthesis of advanced transition metal-based catalyst for hydrogen production via electrolysis of water. *J. Energy Chem.* **57**, 547–566 (2021).
21. Wang, Y., Zhang, B., Pan, W., Ma, H. & Zhang, J. 3 D Porous Nickel-Cobalt Nitrides Supported on Nickel Foam as Efficient Electrocatalysts for Overall Water Splitting. *ChemSusChem* **10**, 4170-4177 (2017).
22. Zhang, B. *et al.* Iron–Nickel Nitride Nanostructures in Situ Grown on Surface-Redox-Etching Nickel Foam: Efficient and Ultrasustainable Electrocatalysts for Overall Water Splitting. *Chem. Mater.* **28**, 6934–6941 (2016).
23. Wu, A. *et al.* Integrating the active OER and HER components as the heterostructures for the efficient overall water splitting. *Nano Energy* **44**, 353–363 (2018).
24. Song, F. *et al.* Interfacing nickel nitride and nickel boosts both electrocatalytic hydrogen evolution and oxidation reactions. *Nat Commun* **9**, 4531 (2018).
25. Lu, Y. *et al.* Bimetallic Co-Mo nitride nanosheet arrays as high-performance bifunctional electrocatalysts for overall water splitting. *Chem. Eng. J.* **411** (2021).
26. Yan, M. *et al.* In situ construction of porous hierarchical $(\text{Ni}_{3-x}\text{Fe}_x)\text{FeN}/\text{Ni}$ heterojunctions toward efficient electrocatalytic oxygen evolution. *Nano Research* **13**, 328–334 (2020).
27. Yu, L. *et al.* Hydrogen Generation from Seawater Electrolysis over a Sandwich-like $\text{NiCoNiNi}_x\text{P}/\text{NiCoN}$ Microsheet Array Catalyst. *ACS Energy Lett.* **5**, 2681–2689 (2020).
28. Yu, L. *et al.* A universal synthesis strategy to make metal nitride electrocatalysts for hydrogen evolution reaction. *J. Mater. Chem. A* **7**, 19728–19732 (2019).
29. Sun, H. M. *et al.* Self-Supported Transition-Metal-Based Electrocatalysts for Hydrogen and Oxygen Evolution. *Adv. Mater.* **32**, 1806326 (2020).
30. Liang, S. Q. *et al.* Nickel-Iron Nitride-Nickel Sulfide Composites for Oxygen Evolution Electrocatalysis. *ACS Appl. Mater. Interfaces* **12**, 41464–41470 (2020).
31. Boppella, R., Tan, J., Yang, W. & Moon, J. Homologous CoP/NiCoP Heterostructure on N-Doped Carbon for Highly Efficient and pH-Universal Hydrogen Evolution Electrocatalysis. *Adv. Funct. Mater.* **29**, 1807976 (2019).
32. Du, X. C. *et al.* Modulating Electronic Structures of Inorganic Nanomaterials for Efficient Electrocatalytic Water Splitting. *Angew. Chem. Int. Ed.* **58**, 4484–4502 (2019).
33. Fan, H. *et al.* Plasma-heteroatom-doped Ni-V-Fe trimetallic phospho-nitride as high-performance bifunctional electrocatalyst. *Appl. Catal. B* **268**, 118440 (2020).
34. Li, R. *et al.* Synergistic Interfacial and Doping Engineering of Heterostructured $\text{NiCo}(\text{OH})_x\text{-Co}_y\text{W}$ as an Efficient Alkaline Hydrogen Evolution Electrocatalyst. *Nano-Micro lett.* **13**, 120 (2021).

35. Li, Y. *et al.* Phosphine vapor-assisted construction of heterostructured Ni₂P/NiTe₂ catalysts for efficient hydrogen evolution. *Energy Environ. Sci.* **13**, 1799–1807 (2020).
36. Xue, Z. *et al.* Interfacial Electronic Structure Modulation of NiTe Nanoarrays with NiS Nanodots Facilitates Electrocatalytic Oxygen Evolution. *Adv. Mater.* **31**, 1900430 (2019).
37. Hu, L. *et al.* Interface engineering for enhancing electrocatalytic oxygen evolution of NiFe LDH/NiTe heterostructures. *Appl. Catal. B* **273**, 119014 (2020).
38. Jiang, H., Hou, Z. & Luo, Y. Unraveling the Mechanism for the Sharp-Tip Enhanced Electrocatalytic Carbon Dioxide Reduction: The Kinetics Decide. *Angew. Chem. Int. Ed.* **56**, 15617–15621 (2018).
39. Liu, M. *et al.* Enhanced electrocatalytic CO₂ reduction via field-induced reagent concentration. *Nature* **537**, 382–386 (2016).
40. Liu, P. *et al.* Tip-Enhanced Electric Field: A New Mechanism Promoting Mass Transfer in Oxygen Evolution Reactions. *Adv. Mater.* **33**, 2007377 (2021).
41. Li, Y. *et al.* Implanting Ni-O-VO_x sites into Cu-doped Ni for low-overpotential alkaline hydrogen evolution. *Nat. Commun.* **11**, 2720 (2020).
42. Anantharaj, S., Karthick, K. & Kundu, S. NiTe₂ Nanowire Outperforms Pt/C in High-Rate Hydrogen Evolution at Extreme pH Conditions. *Inorg. Chem.* **57**, 3082-3096 7b02947 (2018).
43. Zhang, Y. *et al.* Rapid Synthesis of Cobalt Nitride Nanowires: Highly Efficient and Low-Cost Catalysts for Oxygen Evolution. *Angew. Chem. Int. Ed. Engl.* **55**, 8670–8674 (2016).
44. Li, Y. *et al.* Ni/Co-based nanosheet arrays for efficient oxygen evolution reaction. *Nano Energy* **52**, 360–368 (2018).
45. Zhang, N. N. *et al.* Electrochemical Oxidation of 5-Hydroxymethylfurfural on Nickel Nitride/Carbon Nanosheets: Reaction Pathway Determined by In Situ Sum Frequency Generation Vibrational Spectroscopy. *Angew. Chem. Int. Ed. Engl.* **58**, 15895–15903 (2019).
46. Yang, G. C. *et al.* Interfacial Engineering of MoO₂-FeP Heterojunction for Highly Efficient Hydrogen Evolution Coupled with Biomass Electrooxidation. *Adv. Mater.* **32**, 200455 (2020).
47. Gao, X. R. *et al.* Synergizing in-grown Ni₃N/Ni heterostructured core and ultrathin Ni₃N surface shell enables self-adaptive surface reconfiguration and efficient oxygen evolution reaction. *Nano Energy* **78**, 105355 (2020).
48. Zhang, F. F. *et al.* Controlled Synthesis of Eutectic NiSe/Ni₃Se₂ Self-Supported on Ni Foam: An Excellent Bifunctional Electrocatalyst for Overall Water Splitting. *Adv. Mater. Interfaces* **5**, 1701507 (2018).
49. Park, Y. S. *et al.* High-performance anion exchange membrane alkaline seawater electrolysis. *J. Mater. Chem. A* **9**, 9586–9592 (2021).
50. Wu, L. *et al.* Heterogeneous Bimetallic Phosphide Ni₂P-Fe₂P as an Efficient Bifunctional Catalyst for Water/Seawater Splitting. *Adv. Funct. Mater.* **31**, 2006484 (2020).
51. Wang, C. *et al.* Heterogeneous bimetallic sulfides based seawater electrolysis towards stable industrial-level large current density. *Appl. Catal. B* **291**, 120071 (2021).

52. Wang, B. *et al.* Ni_xFe_yN@C microsheet arrays on Ni foam as an efficient and durable electrocatalyst for electrolytic splitting of alkaline seawater. *J. Mater. Chem. A* **9**, 13562–13569 (2021).
53. Chen, H. *et al.* Wood aerogel-derived sandwich-like layered nanoelectrodes for alkaline overall seawater electrosplitting. *Appl. Catal. B* **293**, 120215 (2021).
54. Wu, L. B. *et al.* Rational design of core-shell-structured CoP_x@FeOOH for efficient seawater electrolysis. *Appl. Catal. B* **294**, 120265 (2021).
55. Kumar, A. *et al.* Modulating Interfacial Charge Density of NiP₂–FeP₂ via Coupling with Metallic Cu for Accelerating Alkaline Hydrogen Evolution. *ACS Energy Lett.* **6**, 354–363 (2021).
56. Jadhav, A. R. *et al.* Stable complete seawater electrolysis by using interfacial chloride ion blocking layer on catalyst surface. *J. Mater. Chem. A* **8**, 24501–24514 (2020).
57. Anantharaj, S. & Aravindan, V. Developments and Perspectives in 3d Transition-Metal-Based Electrocatalysts for Neutral and Near-Neutral Water Electrolysis. *Adv. Energy Mater.* **10**, 1902666 (2020).
58. Zou, X. X. & Zhang, Y. Noble metal-free hydrogen evolution catalysts for water splitting. *Chem. Soc. Rev.* **44**, 5148–5180 (2015).
59. Wang, J. H. *et al.* Recent Progress in Cobalt-Based Heterogeneous Catalysts for Electrochemical Water Splitting. *Adv. Mater.* **28**, 215–230 (2016).
60. Yan, H. J. *et al.* Anion-Modulated HER and OER Activities of 3D Ni-V-Based Interstitial Compound Heterojunctions for High-Efficiency and Stable Overall Water Splitting. *Adv. Mater.* **31**, 1901174 (2019).
61. Fernanda J. *et al.* Why are trace amounts of chloride so highly surface-active?. *J. Electroanal. Chem.* **847**, 113128 (2019).

Declarations

Acknowledgments

This work was financially supported by the National Natural Science Foundation of China (21878061), Natural Science Foundation of Heilongjiang Province (YQ2021B004), Open Project of State Key Laboratory of Urban Water Resource and Environment (Grant No QA202138), and the Australian Research Council (DP200100365).

Author contributions

B.W., P.X.Y., S.X.D. and R.P.L. conceived the idea. R.P.L. designed and performed the main experiments and analyzed most of the data including material synthesis, characterization, and electrochemical tests. Q.Y.L. carried out the COMSOL simulation. P.H.R. carried out the DFT calculation. D.W., X.Y.L. and J.Y.M. collected and analyzed the XANES data. Y.H.L. and R.Y.X. helped with COMSOL and DFT analyses. B.W., J.M.X., J.Q.Z., M.Z.A., H.K.L. and S.X.D. provided guidance on characterization and experimental data

analyses. P.X.Y. and B.W. are in charge of the overall project and preparation of the paper. R.P.L. and B.W. co-wrote the original manuscript. All of the authors have discussed the results and revised the paper together.

Competing interests

The authors declare no competing interests.

Figures

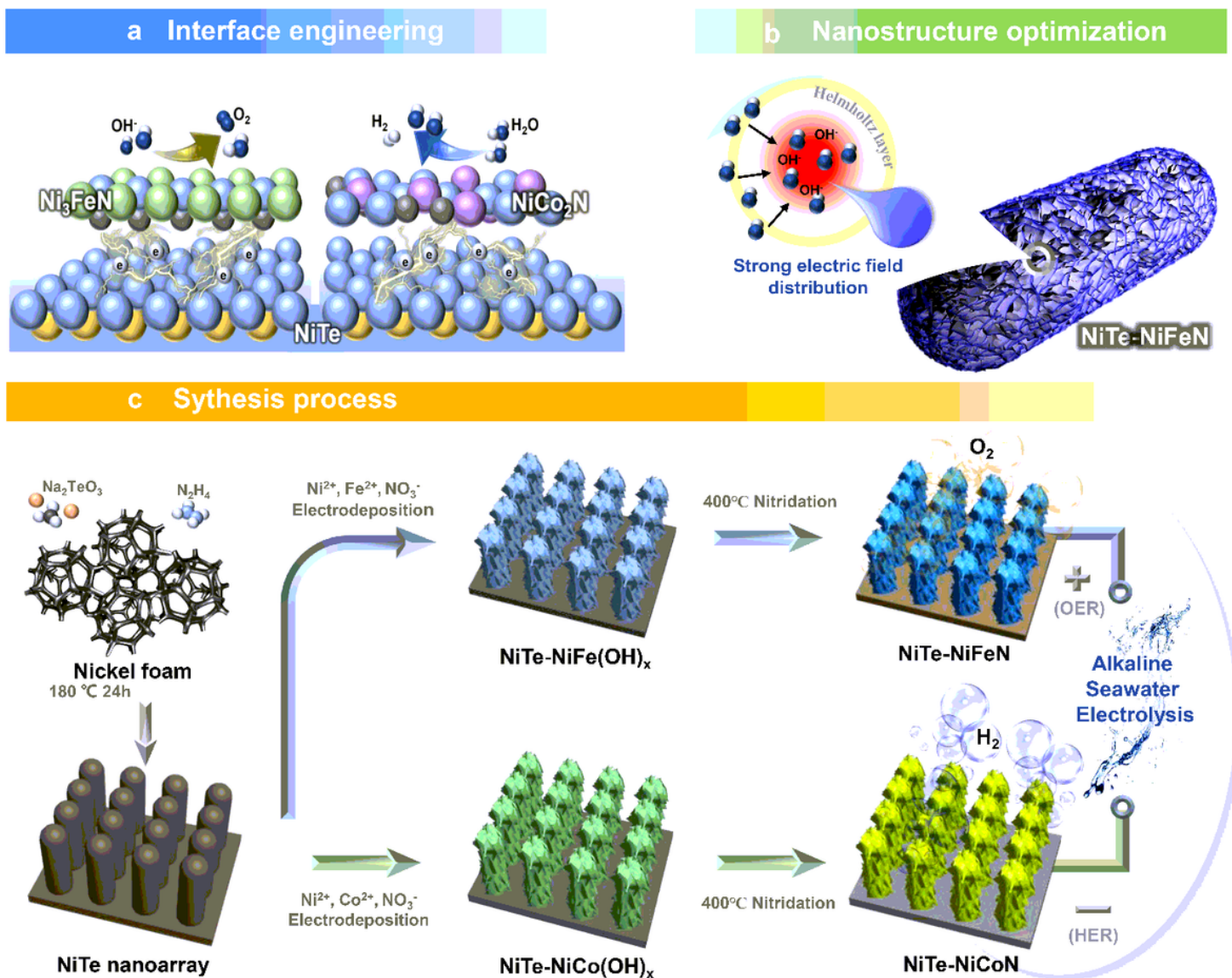


Figure 1

a, b Electrocatalytic activity improvement mechanism of the heterostructured nickel-based tellurium and nitrides. c Schematic illustration of the synthetic processes for the NiTe-NiCoN and NiTe-NiFeN .

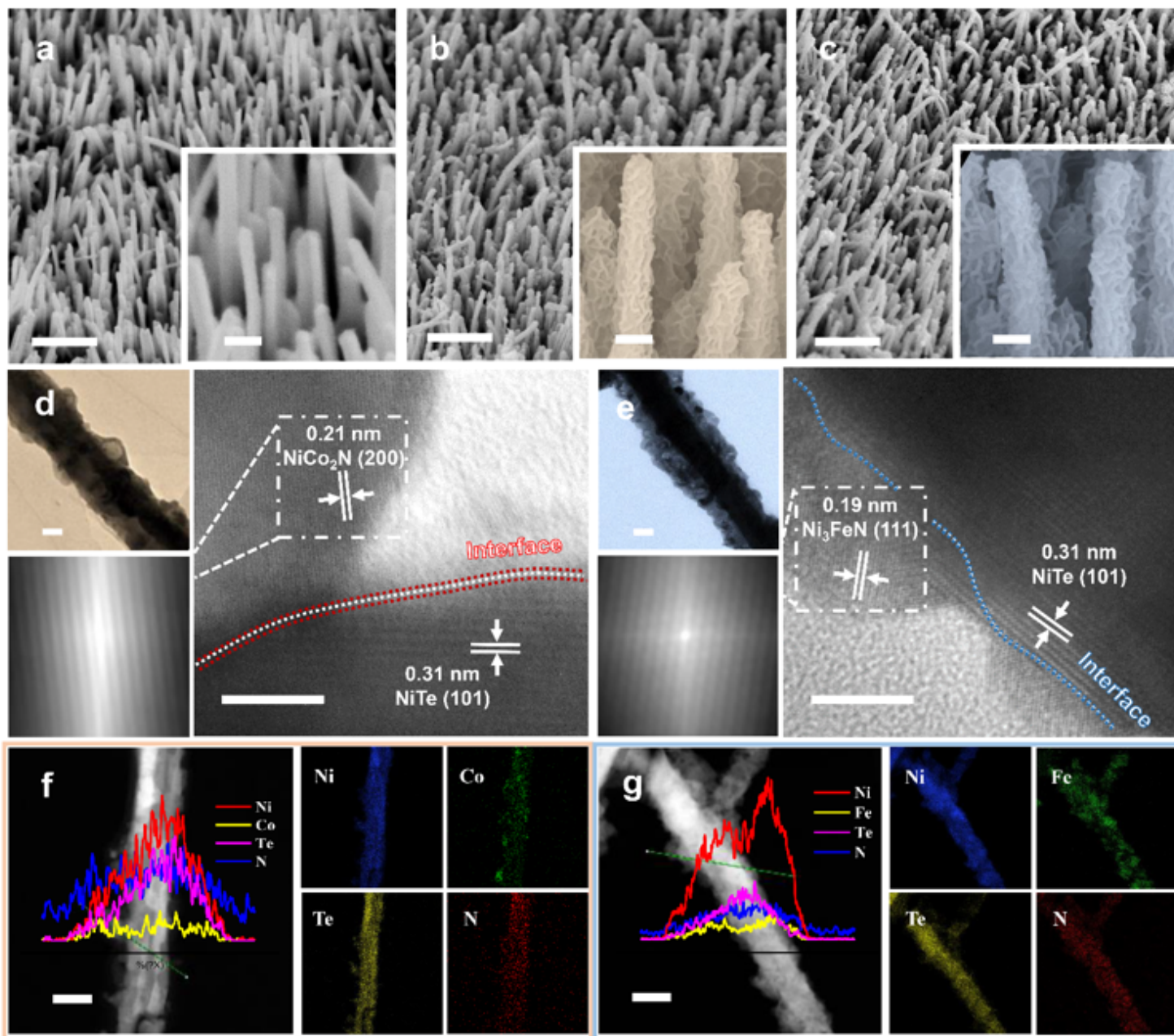


Figure 2

a-c SEM images of NiTe, NiTe-NiCoN, and NiTe-NiFeN. Scale bar, 2 μm (insets: magnified images. Scale bar a 500 nm, b, c 200 nm). d, e TEM and HRTEM images of NiTe-NiCoN and NiTe-NiFeN. Scale bar, 100 nm and 5 nm (insets: partial Fourier transforms). f, g the corresponded HAADF-STEM images and elemental mappings. Scale bar, 200 nm (insets: EDS line scans).

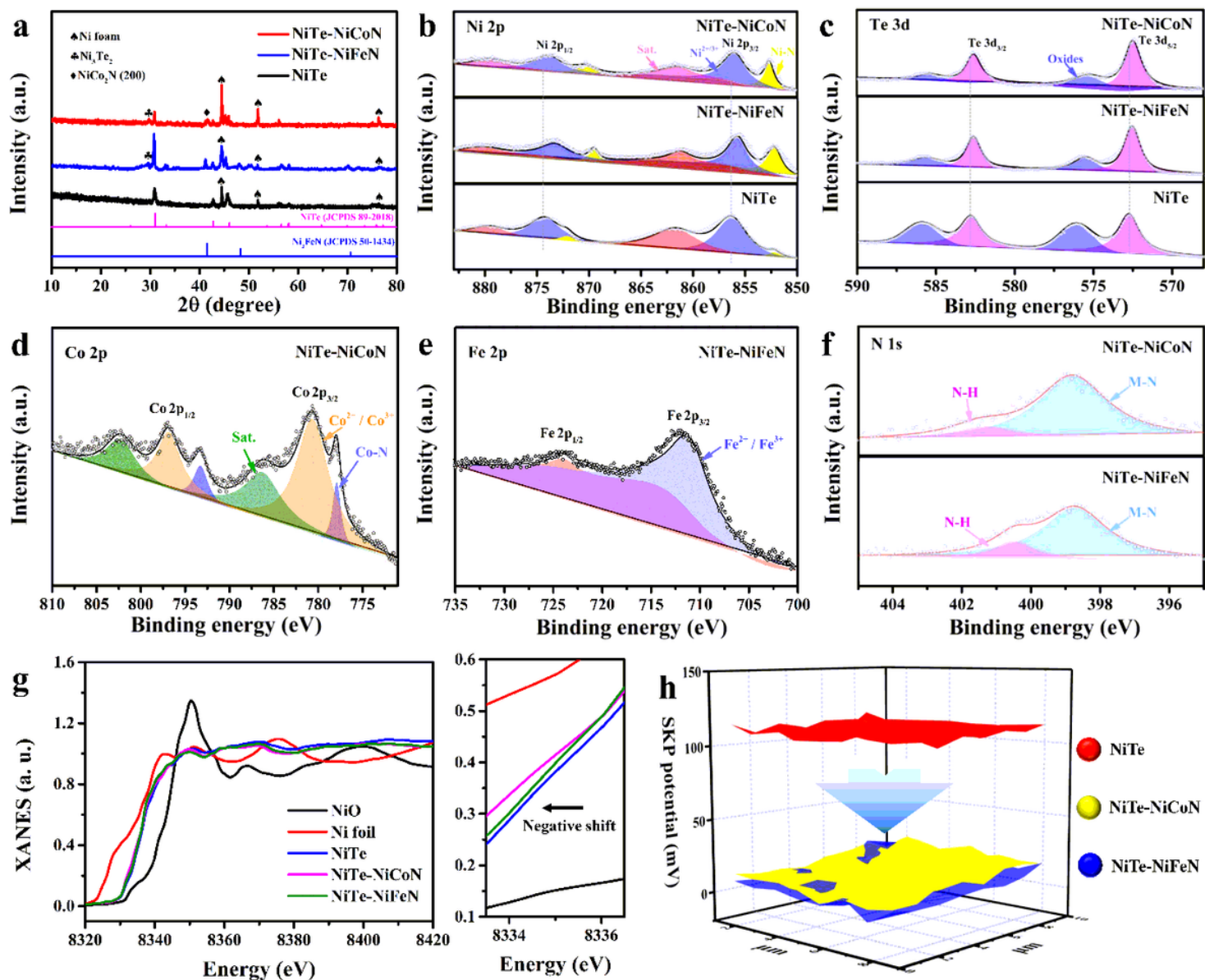


Figure 3

a XRD spectra of NiTe, NiTe-NiCoN, and NiTe-NiFeN. b, c Ni 2p and Te 4f XPS spectra comparing NiTe, NiTe-NiCoN, and NiTe-NiFeN. d, e Co 2p spectra of NiTe-NiCoN and Fe 2p spectra of NiTe-NiFeN, and f the corresponding N 1s spectra. g Ni K-edge XANES spectra for Ni foil, NiO, NiTe, NiTe-NiCoN, and NiTe-NiFeN. h Working function spectra comparison.

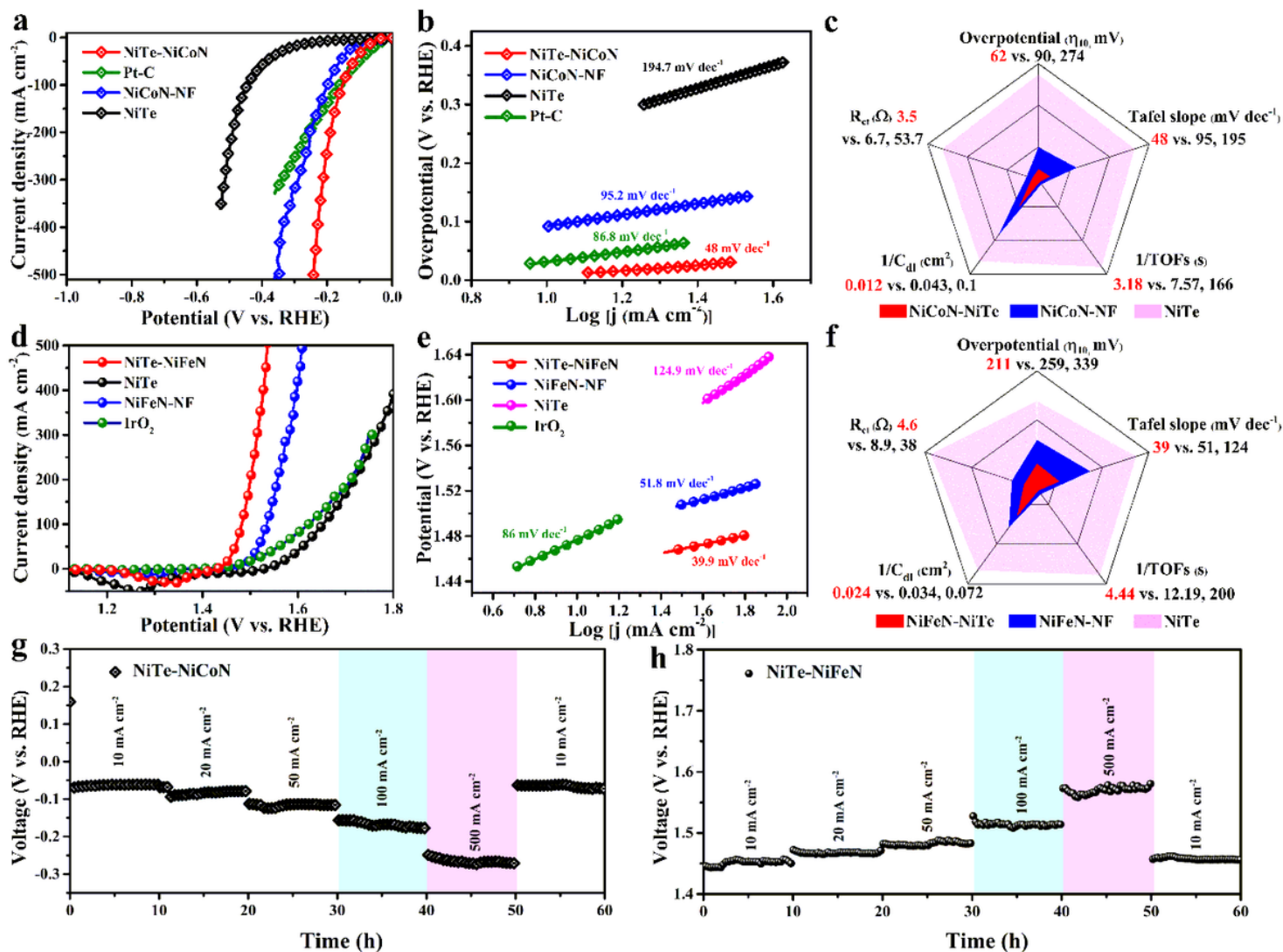


Figure 4

a, b HER polarization curves and Tafel slopes of NiTe, NiTe-NiCoN, NiCoN-NF, and Pt/C. c Integrated HER performance radar chart of the as-prepared samples. d OER polarization curves and e Tafel slopes of NiTe, NiTe-NiFeN, NiFeN-NF, and IrO_2 . f Integrated OER performance radar chart of the as-prepared samples. g, h Chronopotentiometric curves at different current densities (10-500 mA cm^{-2}) of NiTe-NiCoN and NiTe-NiFeN.

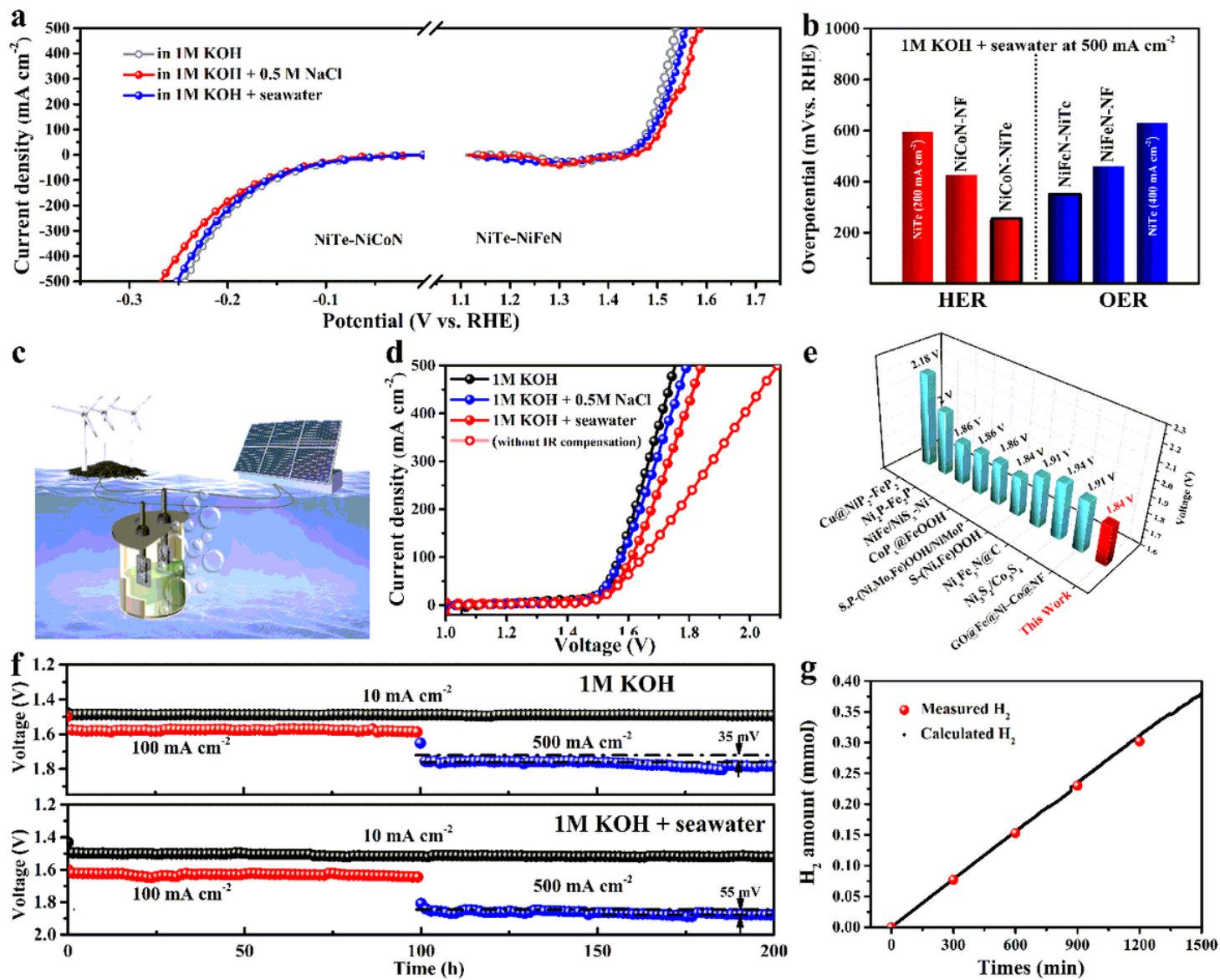


Figure 5

a HER polarization curves of NiTe-NiCoN and NiTe-NiFeN in different media (1 M KOH, 1 M KOH + 0.5 M NaCl, 1 M KOH + seawater). b Comparison of the overpotentials of all the as-prepared samples. c Schematic illustration of an overall seawater splitting electrolyzer that is constructed from NiTe-NiCoN || NiTe-NiFeN and driven by a solar/wind powered system. d LSV curves in different media. e Comparison of electrolysis performance with recent representative works. f Chronopotentiometric curves at different current densities (10, 100, and 500 mA cm^{-2}). g Faraday efficiency of H_2 generation.

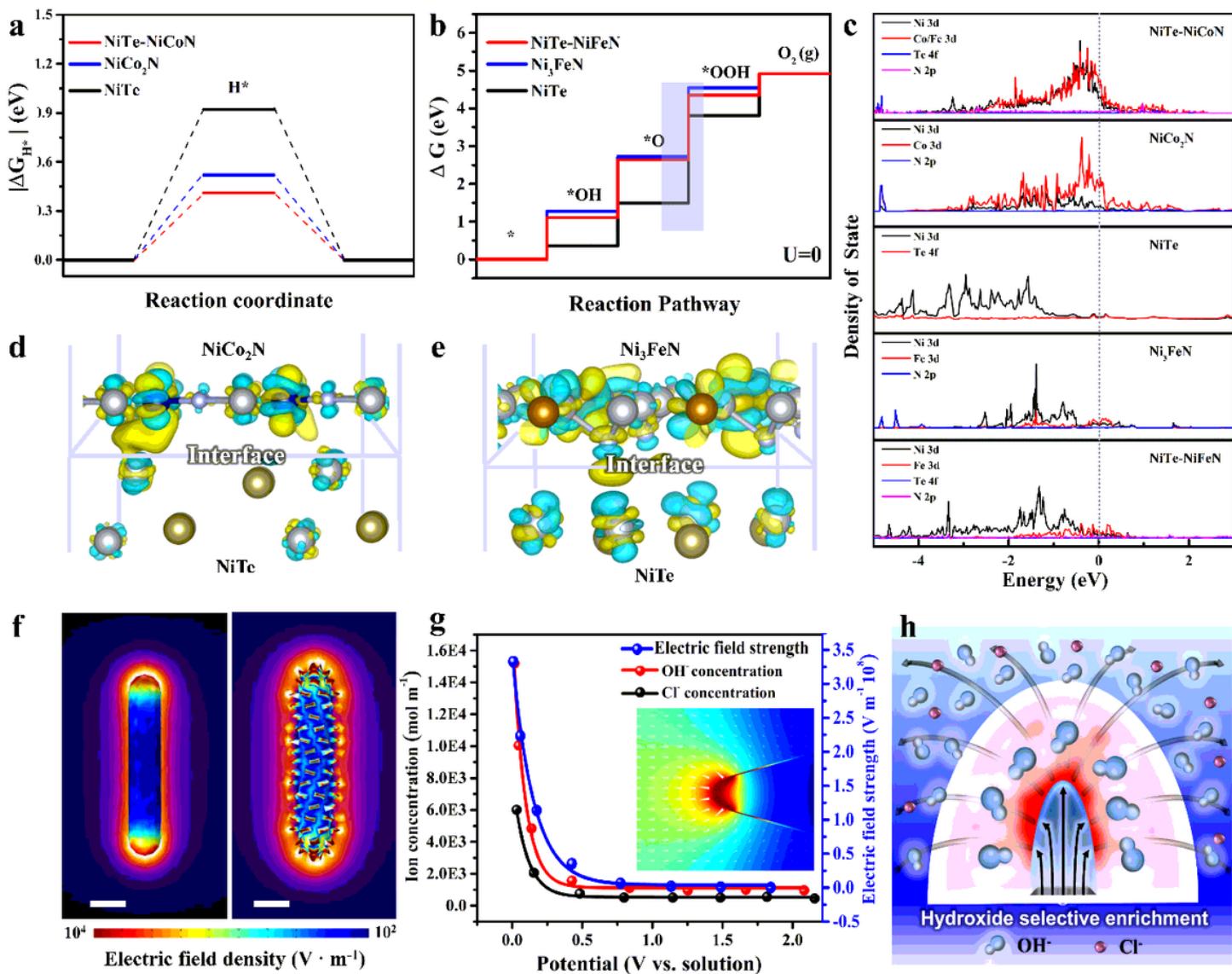


Figure 6

a Free energy diagrams for H⁺ adsorption of heterostructured NiTe-NiCo₂N, NiCo₂N, and NiTe, respectively. b Free energy diagrams at 0 V for the OER process on the heterostructured NiTe-Ni₃FeN, Ni₃FeN, and NiTe, respectively. c Projected density of states comparison of Ni, Co, Fe, Te, and N. d, e The charge density difference in the interfaces of NiTe/NiCo₂N and NiTe/ Ni₃FeN, respectively. f Comparison of electric field distributions with different nanostructures. Scale bar, 200 nm. g The relationship between the different anion concentration distributions (Cl⁻ and OH⁻) and electric field strength versus potential (inset: the calculation area highlighted in the model). h Schematic illustration of the optimal seawater OER mechanism.

Supplementary Files

This is a list of supplementary files associated with this preprint. Click to download.

- [MovieS1.mp4](#)
- [MovieS2.mp4](#)
- [SI20211022.docx](#)